Lithospheric Imaging through Reverberant Layers: Sediments, Oceans, and Glaciers

Ziqi Zhang[1*] and Tolulope Olugboji[1]

[1] *Department of Earth and Environmental Sciences, University of Rochester, NY*

Corresponding author: Ziqi Zhang (ziqi.zhang@rochester.edu)

Key Points

- A data-driven approach using autocorrelation and homomorphic analysis is proposed to detect the signature of reverberations in seismic data
- The proposed approach can be applied to various geological settings where reverberations are present, i.e., sediments, oceans, and glaciers
- Signal enhancement is best in single-layer reverberation systems, while homomorphic analysis is preferred for multi-layer systems

Abstract (limit 250 words)

The Earth, in large portions, is covered in oceans, sediments, and glaciers. High-resolution body wave imaging in such environments often suffers from severe reverberations, that is, repeating echoes of the incoming scattered wavefield trapped in the reverberant layer, making interpretation of lithospheric layering difficult. In this study, we propose a systematic data-driven approach, using autocorrelation and homomorphic analysis, to solve the twin problem of detection and elimination of reverberations without a priori knowledge of the elastic structure of the reverberant layers. We demonstrate, using synthetic experiments and data examples, that our approach can effectively identify the signature of reverberations even in cases where the recording seismic array is deployed in complex settings. For example, using data from (1) the Alaska amphibious community seismic experiment (AACSE), (2) Earthscope transportable array stations deployed in the sedimentary basin around the Mississippi embayment, and (3) stations deployed on ice-sediment strata in the glaciers of Antarctica. The elimination of the reverberation is implemented by a frequency domain filter whose parameters are automatically tuned using seismic data alone. Application of our technique to single stations shows that signal enhancement is best when reverberation is attributable to a single layer. On glaciers where the reverberating sediment layer is sandwiched between the lithosphere and an overlying ice layer, homomorphic analysis is preferable in detecting the signature of reverberation. We expect that our technique will see wide application for high-resolution body wave imaging across a wide variety of conditions.

Plain Language Summary (limit 200 words)

The Earth, in large portions, is covered in oceans, sediments, and glaciers. Because of the large structural difference between these layers and the solid Earth underneath, waves get trapped in them which hampers the successful investigation of deeper layers. This is often referred to as “reverberation” or “resonance" - waves that sound or ‘sing’ again and again. In this study, we propose a systematic approach to detect and eliminate this “singing” effect using only observed data, without any physical knowledge of the local geological structure. Our approach extends the autocorrelation analysis, a widely used method to detect repeating patterns in time series, and also takes advantage of the homomorphic analysis, a popular technique in speech and audio processing. We demonstrate the effectiveness of our approach using both human-

46 generated data and real seismic data, collected from complex geo settings around the world,
47 including in the oceans to the south of the Alaska Peninsula, the Mississippi Embayment, and
48 Antarctica. Application of our approach produces significant signal enhancement in the ocean
49 and sediment environments, where the "singing" effect is simple. We expect that our
50 technique will greatly improve the quality of deep Earth structure investigation across a wide
51 variety of conditions.

1.0 Introduction

The Earth is a water world. As a result, high-resolution body wave imaging of discontinuities across and within its lithospheric shell often involves interpreting data obtained from seismic sensors deployed in the oceans, on the seafloor, or above sediments and glaciers (Anandakrishnan et al., 2000; Clinton et al., 2014; Simon et al., 2021; Suetsugu & Shiobara, 2014; Wiens et al., 2021). However, it is well known that in such conditions, the teleseismic body wavefield can be severely contaminated by reverberations (repeating echoes) generated in these shallowest low-velocity layers, i.e., the water column in oceanic environments (Akuhara & Mochizuki, 2015), sediment layer in both continental and oceanic environments (Audet, 2016; Zelt & Ellis, 1999), or the ice layer in the polar regions (Chaput et al., 2014; Cho, 2011), therefore, hampering the successful application of high-resolution body wave imaging techniques (Audet, 2016; Chaput et al., 2014; Graw et al., 2017; Janiszewski & Abers, 2015; Kumar et al., 2007). Nevertheless, seismic imaging in these environments is essential to improving our understanding of the dynamics of the Earth. For instance, constraints on the elastic structures of the oceanic plates can shed light on their formation and evolution, and help understand how global plate tectonics operates (Kawakatsu & Utada, 2017; Olugboji et al., 2013; Rychert et al., 2020). Additionally, seismic imaging above thick ice sheets, like Antarctica or Greenland, helps provide constraints on the thermal state, and rheology of the lithosphere, all of which have implications for evolution and stability of glaciers (Blankenship et al., 1993; Fahnestock et al., 2001; W. Shen et al., 2018).

Many techniques have been developed to accommodate this difficulty of lithospheric imaging in reverberant environments. They include the model-driven wavefield decomposition techniques (Bostock & Tréhu, 2012; Chai et al., 2017; Langston, 2011; Tao et al., 2014), which require a prior knowledge of the seismic structure of the reverberant layer, and data-driven signal processing techniques, which do not require a priori knowledge of the local seismic structures. The latter techniques generally obtain the signature of reverberations from the time-domain autocorrelation of the source-deconvolved seismograms, i.e., receiver functions (Cunningham & Lekic, 2019; Yu et al., 2015), repeating peaks in the frequency-domain power spectra (Zhang & Olugboji, 2021), or from the comparison of synthetic and observed data (Akuhara et al., 2016; Akuhara & Mochizuki, 2015). In all data-driven methods, the physics and signal processing efforts for removing the effect of the reverberation are very similar; it

involves designing a resonance removal filter parametrized by the reflection coefficient of the bottom interface trapping the wave and the two-way travel time of the wave in the reverberant layer (Backus, 1959; Yu et al., 2015; Zhang & Olugboji, 2021).

In choosing when or how to apply a resonance removal filter, a systematic approach to facilitate the detection of the signature and strength of reverberations is needed, so as to ensure more confident and robust signal enhancement. Such an approach should have the ability to handle the complexities and challenges faced when the seismic structure of the reverberant layer varies in a complicated fashion across the array (Barcheck et al., 2020; Laske et al., 2009; Suetsugu et al., 2018). In the most challenging case where reverberations from multiple layers are expressed, i.e., water column, sediments in the oceans, ice sheets and sediments in the polar regions, the existing signal processing methods may fail to disentangle the signature of reverberations due to the complicated nature of the spectra. Therefore, an approach that can effectively detect and characterize the signature of multiple-layer reverberations is required in such scenarios. Taken together, a proposed technique should be automated, or semi-automated, with minimal intervention of the seismic analyst and unaided by a priori elastic properties of the reverberant layers.

Describing such a method and developing the analytical and associated signal processing tools that show robust utility for lithospheric imaging in reverberant environments is the goal of this work. Our proposed technique is an extension and synthesis of the autocorrelation and homomorphic analysis, with the latter idea borrowing generously from early and recent seismological work in echo detection (Bonner et al., 2002; Buhl et al., 1974; Stoffa et al., 1974) and related ideas in homomorphic speech processing (Bees et al., 1991; Oppenheim & Schafer, 2004; Oppenheim, 1969). Homomorphic analysis, while relatively less common in geophysical signal processing, was introduced for source-side echo detection and single-channel source deconvolution (Bonner et al., 2002; Cohen, 1970; Letort et al., 2016). However, unlike classical and modern echo detection, our application here focuses on its use for the detection of repeating, receiver-side echoes, i.e., reverberations.

Our paper is organized around the two key ideas that are central to our analysis: (1) the automated detection of reverberations, and (2) their elimination using appropriately tuned and

116 robust filter parameters. In the first part on the detection of reverberations, we extend the
117 autocorrelation approach to estimating the presence, strength, and key parameters of the
118 reverberation response. Then, we introduce and apply homomorphic analysis to the refining
119 of the second filter parameter, the echo delay time, especially in the case of a multi-layer
120 reverberation response (i.e., water-sediment and ice-sediment systems). In the second part, we
121 demonstrate the application of the detection and elimination of reverberations using synthetic
122 and real data experiments, showing how our new approach of automatically tuning the
123 resonance removal filters, using seismic data alone, can eliminate the signature of
124 reverberations, even in settings not previously explored. We then discuss how our approach
125 will enable the use of the scattered body wavefield for high-resolution imaging in even more
126 challenging settings around the world.
127
128 **2.0 Method**
129 A seismogram recorded at a station located on or beneath a highly reverberant layer can be
130 seen as a convolution of an earthquake source signal with the impulse response of the receiver-
131 side structures (lithosphere-asthenosphere), and finally the reverberation response of a layer
132 that strongly traps the incoming wave. The strong velocity contrast between the reverberant
133 layer (i.e., water, sediments, and glaciers) and the layer immediately below (i.e., sediment or
134 crust) generates high-amplitude repeating echoes that mask the phases of interest from the
135 crust-mantle boundary or other deeper layers (Figure 1a-b). When the objective is to image
136 the seismic structure beneath the reverberant layer, these trapped waves can be problematic,
137 since they are the strongest signals obscuring any other subsurface conversions and reflections.
138
139 A useful model is to view the reverberations as a generalization of sustained or repeating
140 echoes, that is, waves trapped in a waveguide. The wave transmits into the layer, is reflected
141 perfectly at the top of the layer and is reflected at the bottom repeatedly. In an ideal case, this
142 reverberation response is adequately modeled by a forward resonance filter, which is
143 determined by two parameters: the relative strength of the reverberation, r_0, which is the
144 reflection coefficient at the bottom of the reverberant layer, and the echo delay time, $\tilde{\tau}$, which
145 is the two-way travel time of the waveleg within the reverberant layer. Therefore, a procedure
146 for detection and elimination of the resonance requires identifying these parameters recovered
147 from the seismic signal.

148

149 The first step in reverberation removal is detection. This can be done either by a time-domain
150 autocorrelation analysis or a Fourier-based homomorphic analysis. The autocorrelation
151 technique is simpler and more widely used, so we begin by reviewing its central idea and how
152 it can be extended to detect the presence and strength of the reverberations. In some cases,
153 autocorrelation may fail, due to noisy seismograms or the presence of a hybrid reverberation
154 response (e.g, water-sediment or ice-sediment systems) and can be supplemented by
155 homomorphic analysis. This alternative approach unravels echoes buried in the original signal
156 using a Fourier analysis. It is essential for estimating the echo delay time and has been widely
157 explored in a variety of fields, including audio and speech processing (Deng et al., 2004;
158 Oppenheim, 1969), medical imaging (Wear et al., 1993), and of course, geophysics and
159 seismology (Letort et al., 2018; Scheuer & Wagner, 1985). In our work here, we use it as a
160 supplementary aid to automated echo delay time estimation.

161

162 The signal processing workflow starts with echo detection, then identifying and automatically
163 tuning the reverberation parameters (using both the autocorrelation and homomorphic
164 analysis), and finally ends with resonance removal (Figure 2). If the data does not present
165 strong reverberations, as measured by an echo quality factor, the workflow exits. In this way,
166 the workflow can be used to detect and eliminate reverberations at single station data, or to
167 scan large datasets for signal distortion due to reverberation. In an alternative application, the
168 properties of the reverberating layer, rather than the resonance removal, might be of interest;
169 for example, the goal might be to probe for sediment or ice thickness. In this case, the filter
170 parameters can be used as a set of constraints for estimating the elastic structure of the
171 reverberant layers.

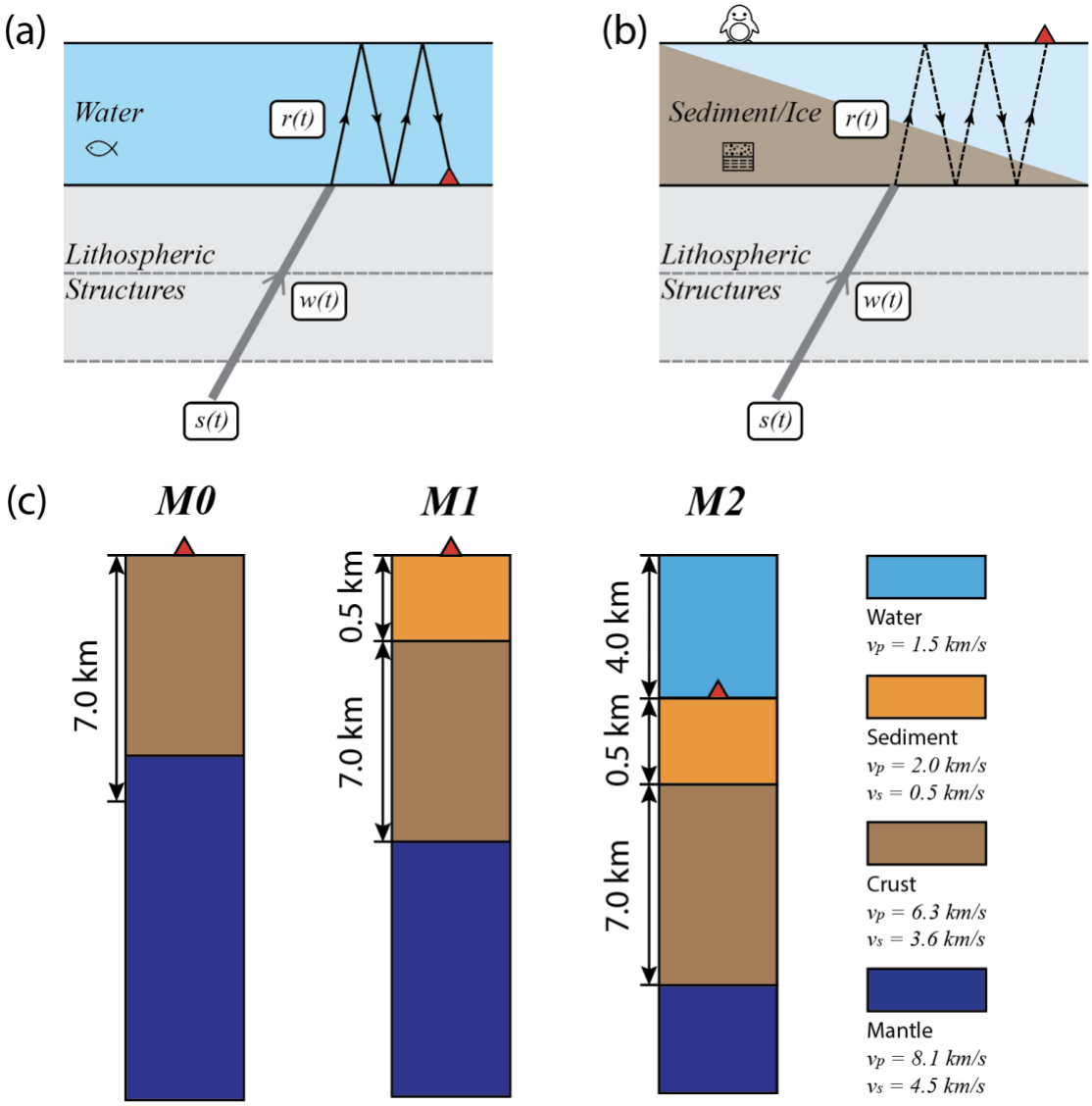

Figure 1. A schematic diagram illustrating how an incoming teleseismic ray is repeatedly reflected in a reverberant setting: (a) water, (b) sediment and ice. Arrows are P (solid) and S (dashed) waves within the reverberating layers and red triangles represent a seismic recording station. *s(t)* represents the source time function; *w(t)* represents the impulse response of the receiver-side lithospheric structure, i.e., Moho, crustal underplating, or lithosphere-asthenosphere boundary (LAB); *r(t)* represents the reverberation response. In submarine environments, a hybrid situation of water and sediment reverberation may exist. In such a case P-waves are trapped in the water layer above and S-waves are trapped in a sediment layer below. Note that for simplicity we have shown *w(t)* as a continuously transmitting P-wave; in reality, it should be interpreted as representing both transmissions, conversions, and reflections, easily obtained from a reflectivity analysis. (c) Velocity models used in synthetic tests. M0: no reverberation, M1: sediment reverberation, M2: water and sediment reverberations. Red triangles indicate station locations.

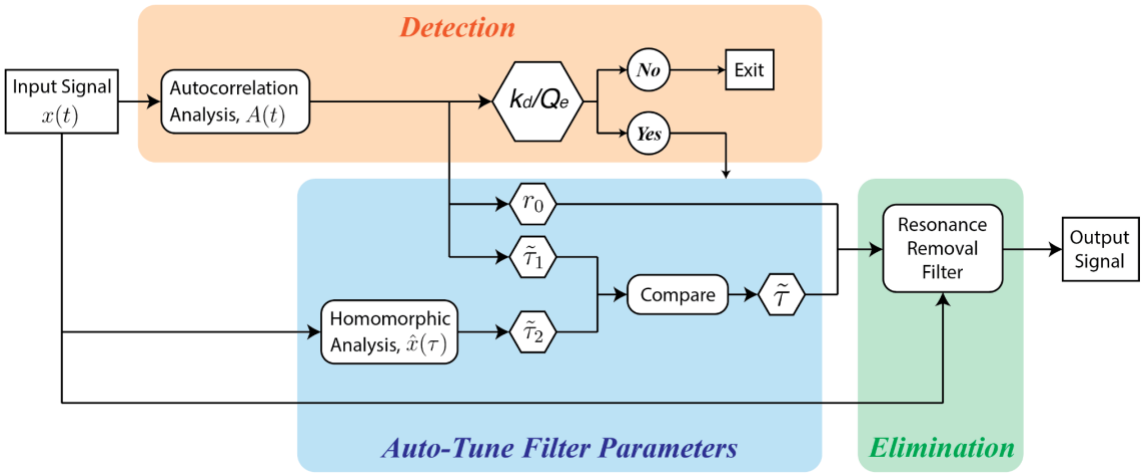

Figure 2. Signal processing workflow for echo detection and elimination proposed in this study. Detection is obtained from an estimate of the echo number, k_d, and the consequent echo quality factor, Q_e. The response of the reverberating layer, characterized by reverberation strength, r_0, and echo delay time, $\tilde{\tau}$, is auto-tuned using autocorrelation and homomorphic analysis. The resonance removal filter is the inverse of the reverberation response and is applied only when repeating echoes (reverberations) are detected.

2.1 Echo Detection with Autocorrelation Analysis

By definition, the autocorrelation function gives the measure of similarity between any signal and its time-delayed version. Therefore, it is easy to see why it is appropriate for detecting the signature of a repeating signal (Phạm & Tkalčić, 2018; Tkalčić et al., 2020). For any input signal $x_0(t)$ that is repeatedly echoed (reverberating), the recorded signal on the seismometer, $x(t)$, and its autocorrelation, $A(t)$, can be written as:

$$x(t) = \sum_{n=0}^{\infty} (-r_0)^n x_0(t - n\tilde{\tau}) \tag{1a}$$

$$A(t) = \int_{-\infty}^{+\infty} x(t)x(t - \xi)d\xi \tag{1b}$$

where $\tilde{\tau}$ is the echo delay time, and ξ is the temporal variable in the autocorrelation integral. The autocorrelation of such a reverberant trace should have the form of a decaying sinusoid, showing a large negative peak with amplitude r_0, at the delay time of the first echo: $n = 1$, $A(t = \tilde{\tau})$. Based on this pattern, (Cunningham & Lekic, 2019) showed that fitting a decaying

sinusoid curve to the autocorrelation function (hereinafter referred to as fitted autocorrelation, A_f) should result in a robust estimation of the filter parameters:

$$A(t) \approx A_f(t) = ce^{-\alpha t} cos \frac{\pi t}{\tilde{\tau}} \quad \textbf{(2)}$$

where t is the lag time of the autocorrelation function, $\tilde{\tau}$ is the half-period of the oscillation (which matches the echo delay time of the input signal), c is the autocorrelation amplitude at zero lag time, and α is the damping factor. The filter parameters can now be estimated from the first trough of the fitted autocorrelation curve (Figure 3b). Previous studies have shown that these parameters can be estimated from a priori knowledge of the elastic structure of the reverberant layer, or may be inferred from empirical measurements obtained from seismic data, i.e., power spectra, coherence between vertical and radial components, and autocorrelation (Yu et al., 2015; Zhang & Olugboji, 2021). Here, we utilize the behavior of the autocorrelation function itself (as captured by Equation 2) to detect the presence and strength of repeating echoes in the seismogram.

The measurement we use here is based on the attenuation response of A_f: the fact that the amplitude of the fitted autocorrelation dies out slowly with strong reverberations and faster with weaker reverberations. We demonstrate this property qualitatively by generating synthetic receiver functions using two different models: with and without a thin sediment layer overlying the crust (models M0 and M1, Figure 1c and Table 1), and calculating the observed and fitted autocorrelation functions (Figure 3). Visually inspecting the results confirms the intuition that the best-fit decaying sinusoid (i.e., the fitted autocorrelation) dies out much more slowly when strong reverberations are present.

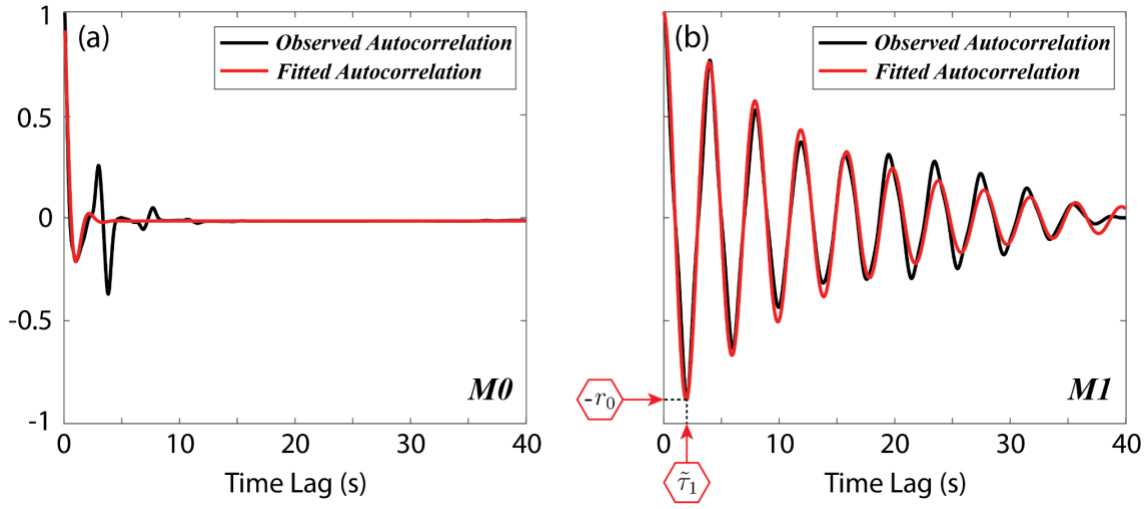

Figure 3. A comparison between the observed and fitted autocorrelation of a synthetic receiver function with and without the presence of reverberation effect. (a) Observed and fitted autocorrelation curves for the case without reverberation, calculated from the model M0. (b) Observed and fitted autocorrelation curves for the case with reverberation, calculated from model M1. Filter parameters, r_0 and $\tilde{\tau}_1$, are obtained from the first trough of the fitted autocorrelation curve.

Table 1. Density, velocity, and thickness parameters of various layers in the synthetic velocity models.

Layer	Density (kg/m³)	Velocity (km/s)		Velocity Ratio	Thickness, H (km)			
	ρ	v_p	v_s	κ	M0	M1	M2	M3
Ice		4.00	2.00	2.00	-	-	-	2.5
Water	1027	1.50	-	-	-	-	4.0	-
Sediment	2000	2.00	0.50	4.00	-	0.5	0.5	0.5
Crust	2800	6.30	3.60	1.75	7.0	7.0	7.0	7.0
Mantle	3200	8.10	4.50	1.80	-	-	-	-

To quantify the strength of a reverberation using the property described above, we define an echo number, k_d, which is a measurement of the number of oscillations it takes for the amplitude of the fitted autocorrelation to drop below a level of $e^{-\pi} = 4\%$ of its amplitude at zero time lag. From Equation 2 we can see that

$$A_{4\%} = A_{t=k_d\tilde{\tau}}$$

$$e^{-\pi} = e^{-\alpha k_d \tilde{\tau}} \cos \frac{\pi k_d \tilde{\tau}}{\tilde{\tau}} \longrightarrow k_d = \frac{\pi}{\alpha \tilde{\tau}} \quad \textbf{(3)}$$

A strong reverberation can then be identified by a simple echo quality factor, Q_e, defined using a user-specified threshold of k_{thr}:

$Q_e = 1$ when $k_d \geq k_{thr}$, indicates strong reverberation (long repeating echoes present)

$Q_e = 0$ when $k_d < k_{thr}$, indicates no reverberation (weak or non-repeating echoes)

We provide a synthetic example to show how k_d and, consequently Q_e, changes when varying the elastic structure of the reverberant sediment layer (Figure 4). We calculate the echo number k_d and the echo quality factor Q_e for a series of synthetic receiver functions generated using a fixed crust and a varying sediment layer. The models used involve increasing the shear velocity and thickness of the sediment layer, such that the echo delay time is fixed at 2.0 s while allowing us to scan the reflection coefficient from 0.8 to 0.2. Note that when the shear velocity and thickness of the sediment reach their highest (3.5 km/s and 3.5 km), the velocity structure of the sediment is almost identical to that of the crust, thus minimizing the reverberation. In this experiment, we see that k_d drops gradually (~22 to 2) as the echo strength (r_0), calculated from the reflection coefficients, decreases from 0.8 to 0.2. Setting the threshold to two echoes, i.e., k_{thr} = 2, results in triggering the echo quality factor on (Q_e= 1) if reverberations are detected and off (Q_e= 0) otherwise. The seismic analyst can specify a more conservative (i.e., higher) value for k_{thr} if detection is required for the strongest reverberations.

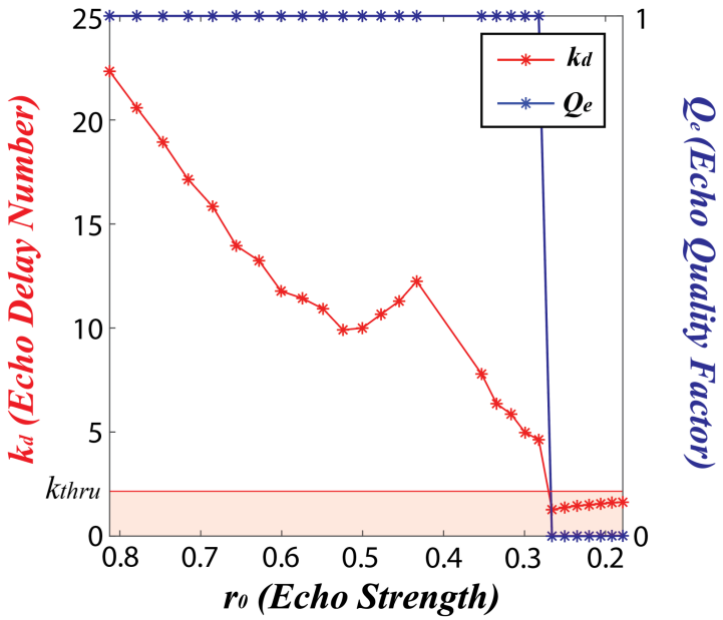

Figure 4. Determining the presence and the strength of reverberation with echo quality factor (Qe). Red and blue curves show relationship between r_0 (reverberation strength) with k_d (echo number) and Qe (echo quality factor), respectively.

2.2 Echo-Delay Time with Homomorphic Analysis

2.2.1 Introduction to Homomorphic Analysis

The treatment of echo detection we just presented is focused on a time-domain representation of the signal. In this presentation, the signature of the repeating echo was successfully obtained from a time-domain measure of similarity of the signal with itself. This is not the only approach for detecting echoes. It turns out that there exists another treatment that makes use of frequency-domain representation of the signals to extract the signature of repeating echoes. This treatment, known as homomorphic analysis, is well documented in classical signal processing (Bogert et al., 1963; Oppenheim & Schafer, 2004) and in early seismology literature as the cepstrum analysis (Stoffa et al., 1974). The key idea is the transformation of signals combined by convolution into new signals combined by addition.

To illustrate the basic principles of homomorphic analysis and the complex cepstrum of any input signal, we reconsider the sampled signal, $x(t)$, which is now composed of a general input wavelet, $x_0(t)$, and a single echo at $\tilde{\tau}$:

$$x(t) = x_0(t) + r_0 x_0(t - \tilde{\tau}) \quad \textbf{(4a)}$$

$$x(t) = x_0(t) * [\delta(t) + r_0\delta(t - \tilde{\tau})] \quad \textbf{(4b)}$$

where r_0 is the reflection coefficient of the echo and $\delta(t)$ is the Dirac delta function. The signal is now viewed as the convolution of the input wavelet with the echo time series. The Fourier transform of such a signal, $x(t) \xrightarrow{\mathcal{F}} \hat{X}(f)$, is given by

$$X(f) = X_0(f)[1 + r_0 e^{-j2\pi f\tau}] \quad \textbf{(5)}$$

and by taking the logarithm of $X(f)$, we recover a new signal

$$\hat{X}(f) = \log X_0(f) + \log[1 + r_0 e^{-j2\pi f\tau}] \quad \textbf{(6)}$$

In this log-spectrum domain, the echo (second term in Equation 6) is an additive periodic component and the inverse Fourier spectrum, $\hat{X}(f) \xrightarrow{\mathcal{F}^{-1}} \hat{x}(\tau)$, of this transformed signal will exhibit a peak at the echo delay time, $\tilde{\tau}$. The output signal, $\hat{x}(\tau)$, which is the homomorphic transform, $x \xrightarrow{\mathcal{H}} \hat{x}$, is the complex cepstrum of the input signal, $x(t)$, and is, by definition, the inverse Fourier transform of the complex logarithm of the Fourier transformed input signal (Bogert et al., 1963; Childers et al., 1977; Oppenheim, 1969). Note that the output can be viewed as being transformed 'back' into a pseudo-time domain, which is called the "quefrency".

2.2.2 Homomorphic Analysis with Synthetic MTC RF

In the extension of homomorphic transform to the general case of a reverberated receiver function trace, $w(t)$, the convolutional model holds:

$$x(t) = w(t) * r(t) = w(t) * \sum_{n=0}^{\infty}(-r_0)^n\delta(t - n\tilde{\tau}) \quad \textbf{(7)}$$

where r_0 and $\tilde{\tau}$ are the reflection coefficient and delay time, respectively. It has previously been shown (Stoffa et al., 1974) that the complex cepstrum of the impulse response of a reverberant layer $r \xrightarrow{\mathcal{H}} \hat{r}$, is given by:

$$\hat{r}(\tau) = \sum_{m=1}^{\infty} (-1)^m \frac{(r_0)^m}{m} \delta(\tau - m\tilde{\tau}) \tag{8}$$

To demonstrate how to identify echoes in a realistic teleseismic waveform using homomorphic analysis, we present a simple example with a simulated radial receiver function, $w_r(t)$. We first generate an artificial radial seismogram, $x_r(t)$, via spike convolution, that is, by summing time-shifted copies of the vertical seismogram, $x_v(t)$, recorded at GSN station PET from an M6.2 earthquake near New Ireland on September 6, 1993 (Figure 5a-b):

$$x_r(t) = x_v(t) * w(t) * r(t) \tag{9}$$

where

$$w(t) = 1.0\delta(t) - 0.8\delta(t-5) + 0.7\delta(t-6) - 0.3\delta(t-7) \tag{10}$$

and $r(t)$ is the impulse response of a reverberant layer specified using ten echoes (n = 10), a reflection coefficient of r_0 = 0.6, and an echo delay time of $\tilde{\tau}$ = 2.0 s. The radial receiver function, $w_r(t)$, is then calculated using the MTC (multi-taper correlation) algorithm (Park & Levin, 2000; 2016) (Figure 5c). The complex cepstrum is then estimated by homomorphic transform: $w \xrightarrow{\mathcal{H}} \hat{w}$. Buried in the power cepstrum of $\hat{w}$ is the reverberation response, $\hat{r}$, visible as spectral peaks.

For clearer identification of these peaks, a high-pass filter (i.e., linear filtering on the log spectrum) is applied to $\hat{w}$, in order to whiten its spectrum and amplify the resonance response. Despite the unique source spectrum in the vertical seismogram, the complex cepstrum of the echoed receiver function, $\hat{w}$, clearly shows a negative peak at 2.0 s ($\tilde{\tau}$) and a positive peak with a lower amplitude at 4.0 s ($2\tilde{\tau}$), which indicates the successful detection of the reverberation response (Figure 5d).

To accurately determine the echo delay time ($\tilde{\tau}$) from the complex cepstrum, $\hat{w}$, we apply a linear stack with Gaussian smoothing windows at different time intervals:

$$S(\tau) = \sum_i \sum_j \gamma_j G(j\tau_i) \hat{w}_r(\tau) \tag{11}$$

where j is the number of delay times (i.e., peaks in the complex cepstrum trace) used in the

stack, γ_j is the corresponding weighting factors, $G(j\tau_i)$ is the jth window centered at the ith delay time, and $\hat{w}$ is the complex cepstrum of the receiver function trace.

In our implementation, we use the first three peaks (i.e., j=1, 2, 3) and set the weighting factors, γ_j, to -0.6, 0.3, -0.1, respectively. The theoretical resonance quefrencies calculated from the two-way travel time match the first few peaks and troughs of the cepstrum curve (dashed lines in Figure 5d). Note that the absolute amplitudes of the peaks and troughs in the power cepstrum gradually decay as quefrency grows. Since the cepstral peaks are already clearly visible at a 2.0 s interval, there is no surprise that the stack, $S(\tau)$, is maximum at echo-delay time $\tilde{\tau}$ = 2.0 s (Figure 5e).

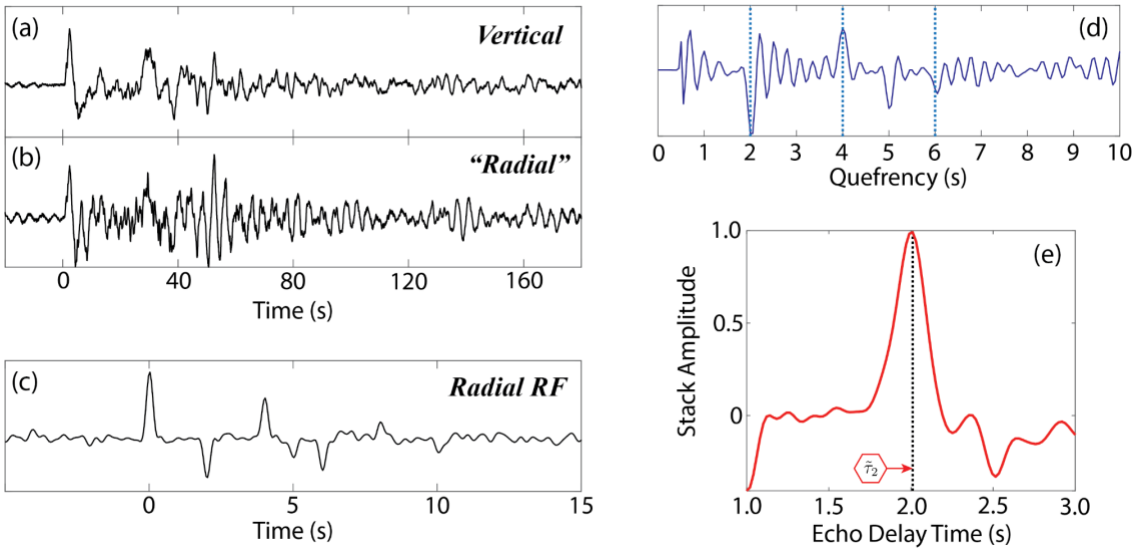

Figure 5. Homomorphic Analysis with MTC (Multi-Taper Correlation) receiver functions. (a) Vertical seismogram recorded at GSN station PET from an M6.2 earthquake near New Ireland on September 6, 1993. (b) Artificial radial seismogram generated by convolving the vertical record with the prescribed spike series and the echo impulse response, and adding the additive noise. (c) MTC (multi-taper correlations) RF (receiver functions) from reverberated radial seismograms shown in Figure 5b. (d) Complex cepstrum of reverberated RFs shown in Figure 5c. (e) Delay time stack of the reverberated RF cepstrum shown in Figure 5d.

2.2.3 Homomorphic Analysis with Synthetic RFs

We carry out a similar analysis using synthetic RFs generated with realistic layered models consisting of water and sediment reverberations using the reflectivity technique. In the single-layer case where the reverberation is generated solely from a sediment layer (M1, Figures 1c

and Figure 6a), the echo delay time of ~ 2.0 s is clearly detected in the complex cepstrum (i.e., $\tilde{\tau}$ = 2.0 s, $2\tilde{\tau}$ = 4.0 s, $3\tilde{\tau}$ = 6.0 s, Figure 6b). Consequently, the stack, $S(\tau)$, for echo delay time gives an accurate result of 2.0 s (Figure 6c). In the hybrid case , in which the reverberations are generated from both a water column and a sediment layer (M2, Figures 1c & 6d), two sets of repeating cepstrum peaks can be observed, corresponding to reverberations from sediment and water, respectively ($\tilde{\tau}_s$ = 2.0 s and $\tilde{\tau}_w$ = 5.3 s, Figure 6e). Since the echo delay times are distinct, applying the stack with two different search windows (1.0 s to 3.0 s for sediment and 4.0 s to 6.0 s for water) recovers both echo delay times (Figure 6f-g). In additional tests with noise added to the RF traces, the cepstral traces are noisier and while the signature echoes are harder to visually identify, they can still be estimated by $S(\tau)$ (see Figure S1 in supporting information). In cases where the goal is to recover the signature of more than one reverberant layer, the homomorphic analysis is the preferred approach so long as the echo-delay times of the layers are well separated.

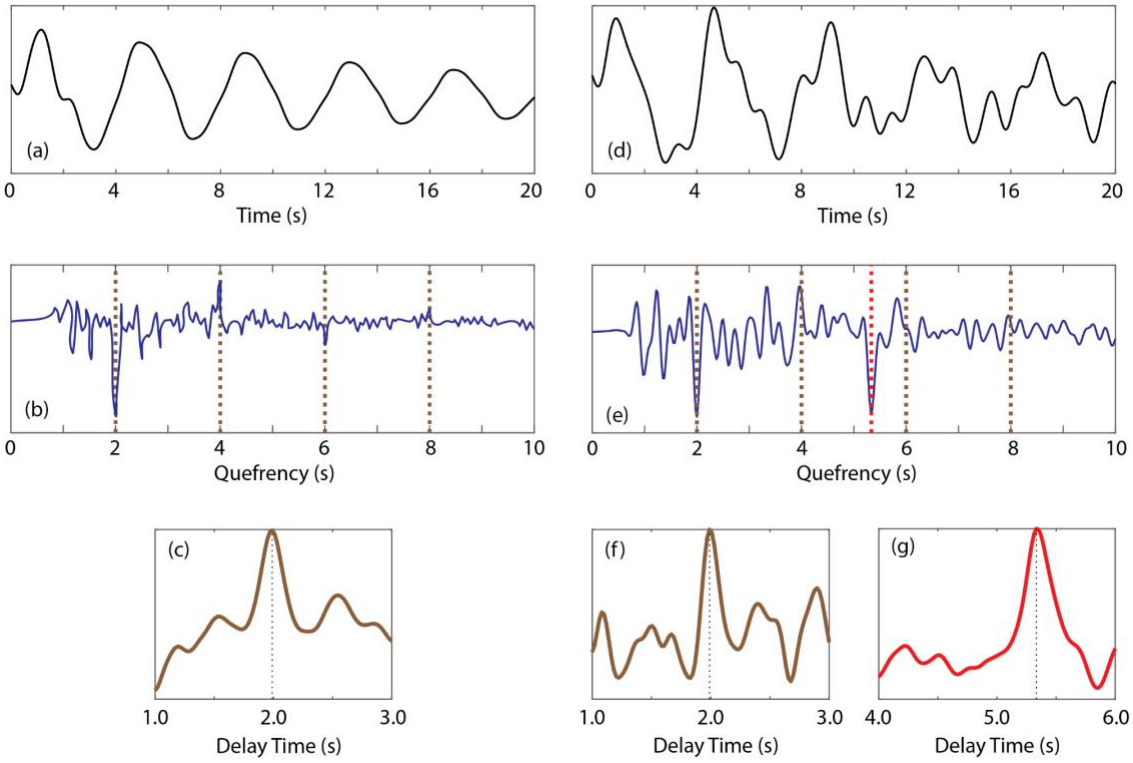

Figure 6. Homomorphic analysis of synthetic receiver function calculated from (a-c) models M1 and (d-g) M2. (a) Synthetic RF from model M1. (b) Complex cepstrum of the synthetic RF shown in Figure 6a. Brown dashed lines indicate the sediment echo delay time. (c) Delay time stack for complex cepstrum shown in Figure 6b. (d) Synthetic RF from model M2. (e) Complex cepstrum of the synthetic RF shown in Figure 6d. Brown dashed lines and the red dashed line indicate the sediment and water echo delay times, respectively. Note that only the first negative peak of the water echo delay time is visible because of the

quefrency axis limit. (f-g) Delay time stack for sediment and water reverberations using the complex cepstrum shown in Figure 6e, respectively.

2.3 Frequency Domain Resonance Removal Filter

After the signature of the reverberations has been determined using the described autocorrelation and homomorphic analysis, it can hen be removed from the contaminated signal by building a resonance removal filter in the frequency domain:

$$F(f) = 1 + r_0 e^{-i2\pi f\tilde{\tau}} \quad \textbf{(12)}$$

where r_0 and $\tilde{\tau}$ are the estimated reverberation strength and echo delay time, respectively. Note that $\tilde{\tau}$ is the same two-way travel time of a reflected wave in a trapped layer and with the right substitution, gives the well known equation for the resonance frequency:

$$f_k = \frac{(2k-1)}{2\tilde{\tau}} \quad \text{where} \quad \tilde{\tau} = 2\frac{d_l}{v_l} \quad \textbf{(13)}$$

where d_l and v_l are the thickness and velocity of the reverberant layer. However, in this case, we do not need to know the elastic structure of the reverberant layer, since the echo delay time, $\tilde{\tau}$, is obtained from time-domain autocorrelation, homomorphic analysis, or both (Figure 2). We refer the readers to (Zhang & Olugboji, 2021) for a more comprehensive discussion on the design and robustness of the filter. Here, we note that both parameters are reliably recovered by the seismic data alone, without need for a model.

3.0 Applications to Seismic Data on Sediments and Oceans

We demonstrate, using both single station and seismic array data, that our proposed workflow can effectively identify the presence of reverberations in the teleseismic body-wave signals.

3.1 Single Station Detection and Removal: Sediments (NE68)

We choose a station located in the Songliao basin, northeast China (NE68), which has been previously studied by (Yu et al., 2015). We obtain 195 teleseismic events with magnitudes larger than Mw 6.0, located 30 to 90 degrees away from station NE68, and calculate the

receiver function (RF) traces using the MTC (multi-taper correlation) approach, using a cutoff frequency of 1.0 Hz (Figure 7a). The autocorrelation analysis shows strong similarity between the observed and fitted autocorrelation curves at the first few oscillations, and gives an echo number, k_d = 9.83, and consequently an echo quality factor of Q_e= 1 (Figure 7b). Based on the discussion in section 2.1, we determine that sediment reverberation is present in the calculated RFs. We then calculate the complex cepstrum of the RFs and use it to estimate the stack, $S(\tau)$ (Figure 7c-d). The reverberation responses (r_0 = 0.69; $\tilde{\tau}_1$ = 1.31 s and $\tilde{\tau}_2$ = 1.33 s, $\tilde{\tau}$ = 1.32 s) are obtained from the autocorrelation and homomorphic analysis of the receiver function signal. The frequency-domain resonance removal filter, designed using these parameters, is then applied to the original RFs to generate the filtered RFs (Figure 7e).

After deconvolution of the reverberation response, the direct Ps conversion from the Moho (the first red vertical line) is clearly visible at around 5.0 s compared to the original RFs, in which the conversion phase is completely buried in the reverberations (Figure 7a). Note that the amplitudes of the following multiples (the second and third red vertical lines) are relatively small due to the high amplitude of the PbS phase (i.e., Ps conversion at the sediment-crust boundary) at around 1.0 s in the filtered RF (Figure 7e). Nevertheless, the $H-\kappa$ stacking (using a crustal P velocity of 6.4 km/s (Tao et al., 2014) can still take advantage of the moveout information and gives a clear result. Our obtained crustal thickness (35.0 km) and P-to-S velocity ratio (1.73) are consistent with those obtained by (Yu et al., 2015), who reported a crustal thickness of 35.2 km and a P-to-S velocity ratio of 1.74.

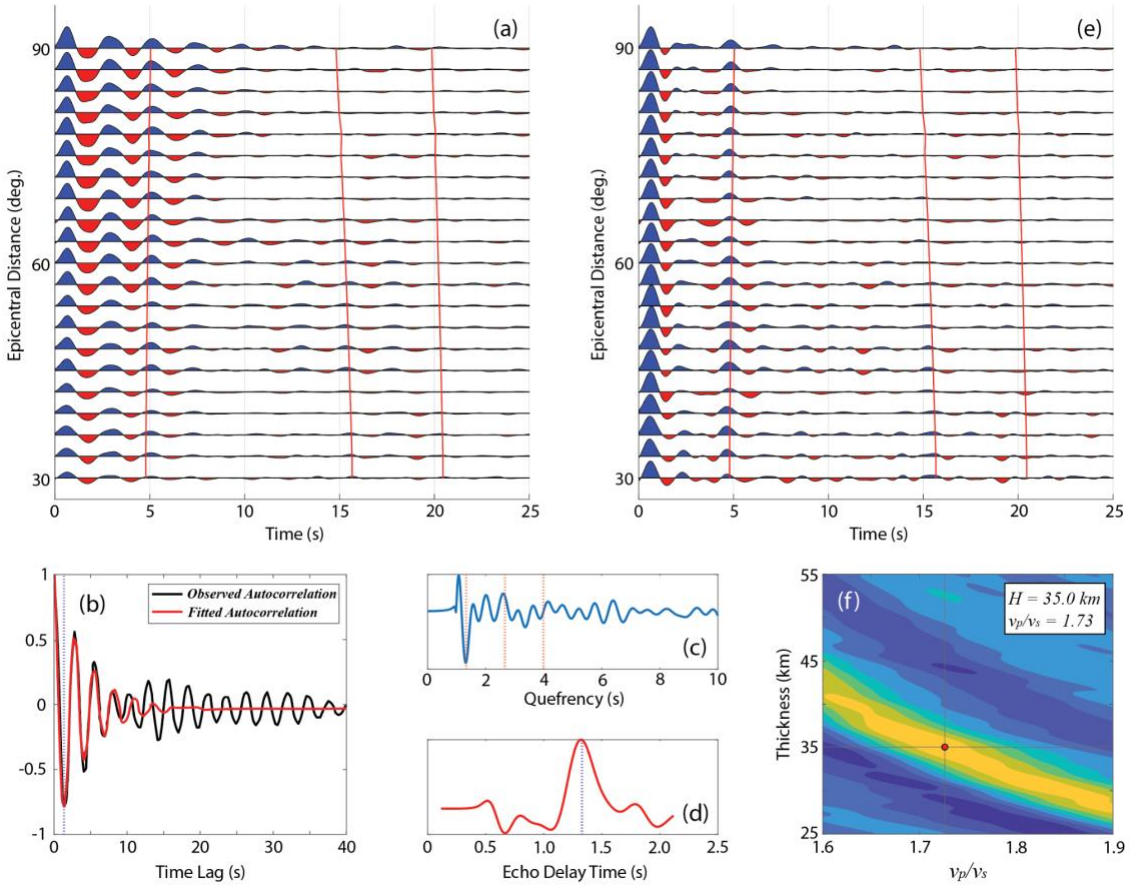

Figure 7. Application of the echo detection and elimination workflow to teleseismic data recorded at station NE68. (a) Original RFs plotted against epicentral distance. Red vertical lines indicate the estimated arrival times for Ps conversion at the Moho and its multiples. (b) Observed and fitted autocorrelation functions. The blue dashed line indicates the echo delay time determined from the autocorrelation analysis. (c) Complex cepstrum of the original RFs. (d) Delay time stack of the complex cepstrum. The blue dashed line indicates the echo delay time determined from the homomorphic analysis. (e) Filtered RFs plotted against epicentral distance. (f) $H - \kappa$ stacking using the filtered RFs.

3.2 Echo Detection on Sedimentary Basins: The Upper Mississippi Embayment

The second example we turn to is the Earthscope transportable array around the Upper Mississippi Embayment, located near the New Madrid seismic zone (Figure 8). Again, this is a region whose crustal structure has previously been investigated by (Liu et al., 2017) using receiver function and gravity constraints. In their investigation, they applied resonance removal filters to some of the stations, to obtain more reliable reflectivity images, however, it was unclear why the stations were chosen. In this case study, we apply the detection module of our FADER workflow (Figure 2) to receiver functions calculated from teleseismic data recorded at 31 stations of the Transportable Array (TA) of the USArray project in the study area, to determine the presence and strength of the sediment reverberations. The calculated

453 echo number, k_d, ranges from 1.08 to 9.10 across the region, with most of the stations
454 expressing the strongest reverberations located inside the Upper Mississippi Embayment,
455 particularly to the east of the study area. We are able to match, with accuracy, all stations where
456 (Liu et al., 2017) detects reverberations. However, we also observe some stations to the west
457 of the UME with notable reverberations, which may benefit from a reconsideration in future
458 imaging efforts (see Table S1 in supporting information for a compilation of the reverberation
459 response).

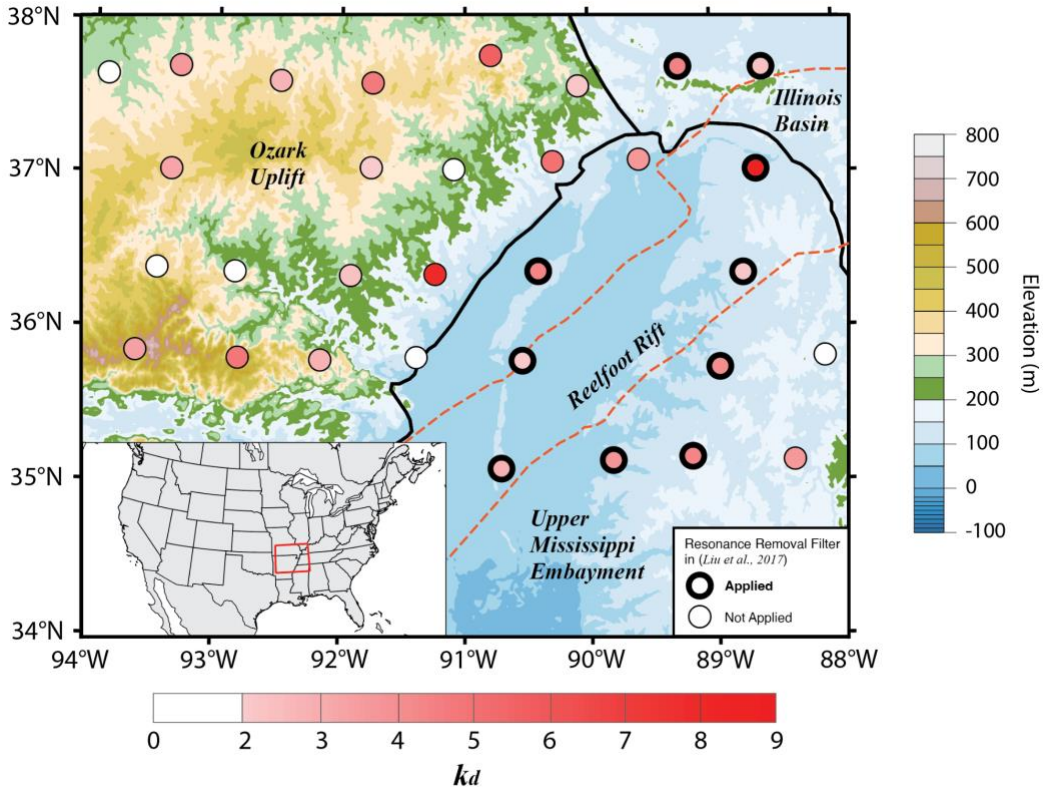

460

461 **Figure 8**. Echo detection in and around the Upper Mississippi Embayment. Major tectonic features are shown in black lines;
462 the location of the Reelfoot Rift is marked in orange dashed lines. Stations expressing strong reverberation, as detected by
463 (Liu et al., 2017), are identified by thick boundaries (thin line otherwise); the color of the circles indicates k_d values obtained
464 in this study.

465 **3.3 Echo Detection on a Submarine Array: The Alaska Experiment**

466 A third example is taken from another seismic array, but one located in the oceans and not on
467 land (model M2 of Figure 1c). This is a seismic array crossing from deep oceans into shallow
468 oceans, deployed across the subducting pacific plate. The Alaska Amphibious Community

Seismic Experiment (AACSE) presents a unique opportunity to conduct high-resolution seismic imaging of the lithosphere-asthenosphere system of the Pacific plate, prior to subduction (Barcheck et al., 2020). This is only possible if the reverberation response can be modeled successfully. We obtain teleseismic data, and calculate receiver functions, using data from fifty ocean bottom seismometers (OBS) of the AACSE array. The echo number, k_d, obtained from autocorrelation analysis, ranges from 0.78 to 13.04, across the array. An echo threshold, $k_{thr} = 2$, suggests that reverberations exist at over half of the stations (Figure 9). A comparison of the measured echo delay times, with predicted water reverberations, at stations expressing the strongest reverberations, suggests that the reverberations are from the sediment layer underneath the stations and not from the water-layer above (see Figure S2 in supporting information). This is a promising evaluation because it allows the straightforward deconvolution of the reverberation response, following careful estimation of the relevant parameters of a single sediment layer.

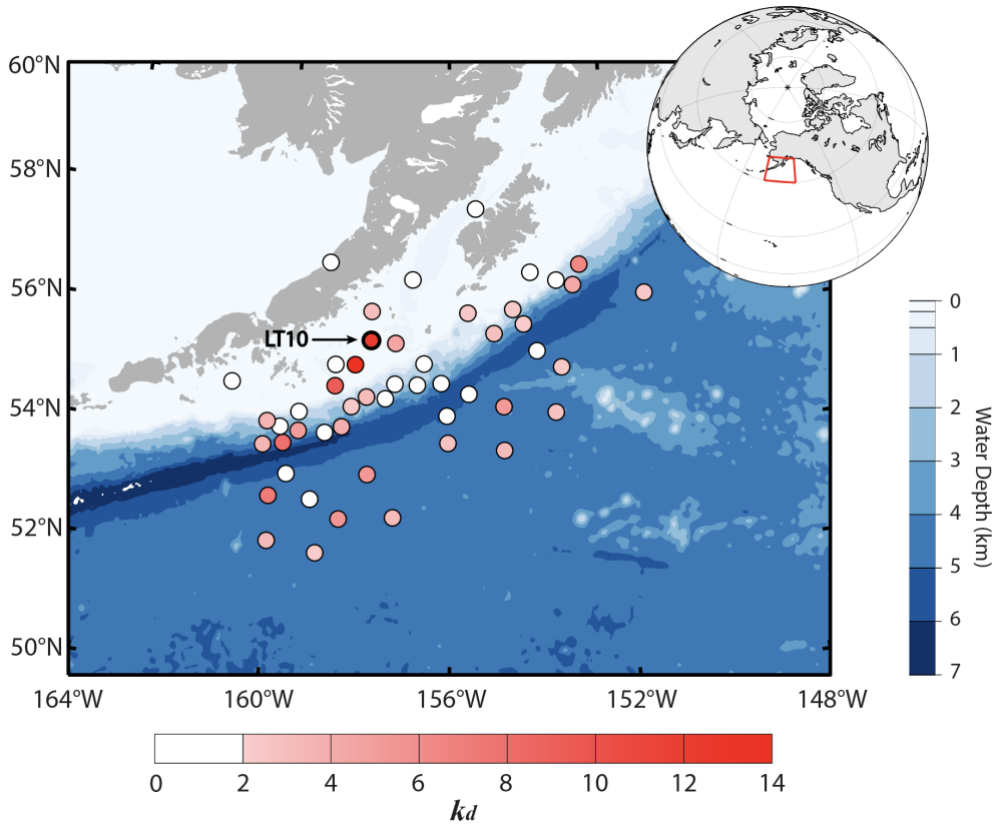

Figure 9. Echo detection in the Aleutian subduction zone. Circles denote OBS locations and the color of the circles indicates k_d values. Station LT10 is highlighted for further analysis in Figure 10.

Here we present an example demonstrating the detection and elimination of reverberations for one of the most reverberant stations on AACSE (LT10). We obtain 115 teleseismic events with magnitudes larger than Mw 6.0, located 30 to 90 degrees away from the station, and calculate the receiver function (RF) traces using the MTC (multi-taper correlation) approach, using a cutoff frequency of 1.0 Hz (Figure 10a). Using autocorrelation and homomorphic analysis, we determine an echo delay time of $\tilde{\tau}$ = 1.63 s and a reverberation strength of r_0 = 0.47 (Figure 10b-d). After resonance removal, the coherence of later-arriving phases are improved in the filtered RFs, with clear detection of lithospheric conversions and their multiples significantly enhanced. For example, a strong and clear arrival at ~ 3 s (Figure 10e) is observed. The $H - \kappa$ stacking using an average P velocity of 6.3 km/s (Eberhart-Phillips & Christensen, 2006) gives a layer thickness of 19.4 km/s and a velocity ratio of 1.76 (Figure 10f). We interpret this to be the boundary of the middle crust and an ultramafic-mafic lower crust, as previously detected by wide angle active source imaging (Shillington et al., 2004). The signature of this layer had previously been obscured and illustrates why interpretations of the teleseismic body-wavefield should be treated with caution when the possibility of distortions from reverberations are not accounted for.

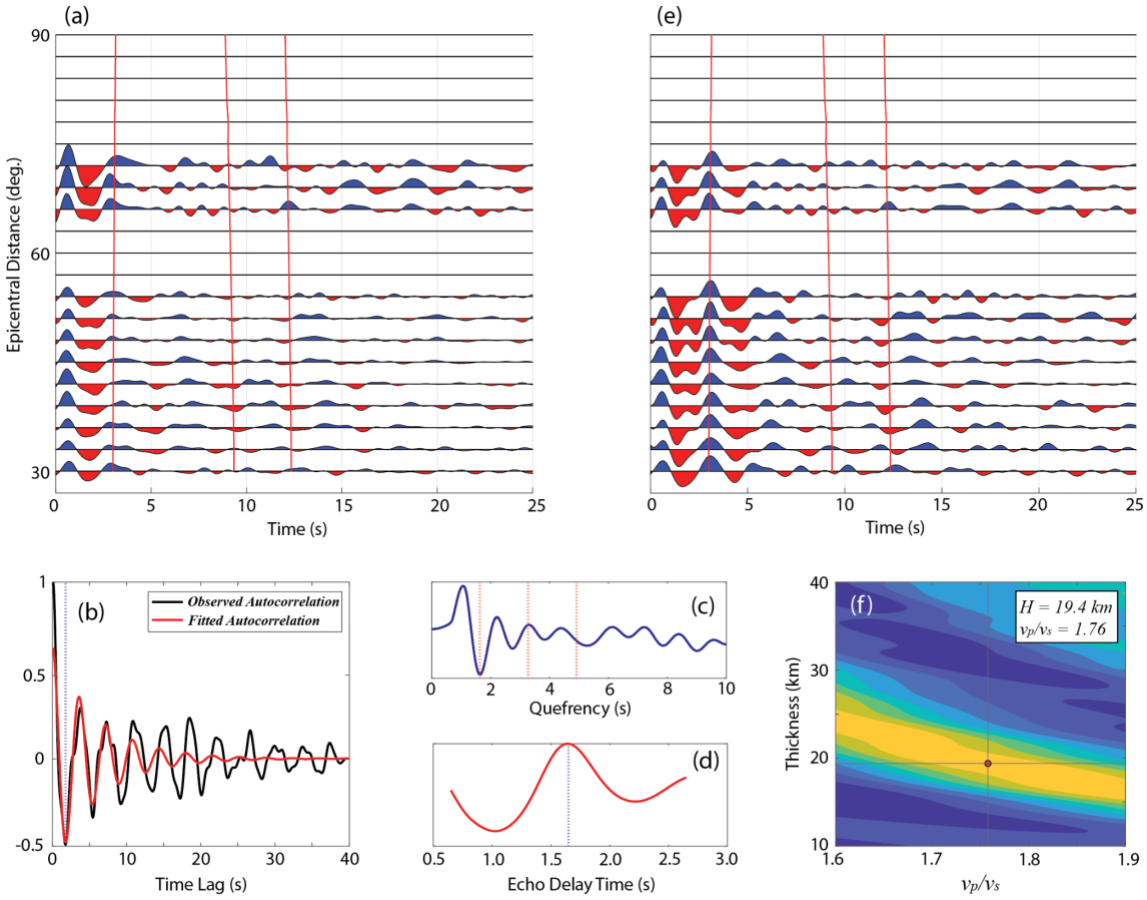

Figure 10. Application of the echo detection and elimination workflow to teleseismic data recorded at station LT10 located in the Aleutian subduction zone. (a) Original RFs plotted against epicentral distance. Some epicentral distance bins do not have RF traces due to the lack of events. Red vertical lines indicate the estimated arrival times for Ps conversion at the interface detected and its multiples. (b) Observed and fitted autocorrelation functions. The blue dashed line indicates the echo delay time determined from the autocorrelation analysis. (c) Complex cepstrum of the original RFs shown in Figure 10a. (d) Delay time stack of the complex cepstrum. The blue dashed line indicates the echo delay time determined from the homomorphic analysis. (e) Filtered RFs plotted against epicentral distance. (f) $H - \kappa$ stacking using the filtered RFs.

4.0 Echo Detection When Both Ice and Sediment is Present

We now turn to a more complicated setting where reverberations are generated from both an ice layer and a sedimentary layer. Although similar, at first sight, to the previous example, one major difference between the water-sediment and the ice-sediment response is that in the former case, for submarine deployments, the station is sandwiched between the two layers (model M2, Figure 1c), while in the latter case it is located on top of the two layers: ice-sediment (model M3, Figure 11a). In the water-sediment system, reverberations from the two layers are distinct and decoupled, arriving separately at the station, enabling the homomorphic analysis to detect two distinct echo delay times (Figure 6e-g). In the ice-sediment system,

however, the station is on top of the ice layer, and the reverberations are now mixed, expressed as a sum (in the homomorphic signal) of the combined effects of the ice and the sediment layers.

We demonstrate this using synthetic RFs generated for layered model M3, which consists of both ice and sediment layers (Figure 11a). In this model, the two-way travel times (i.e., echo delay times) within the ice and sediment layers are $\tilde{\tau}_i$ = 2.5 s and $\tilde{\tau}_s$ = 2.0 s (calculated from Equation 13). The reverberation response of the ice and sediment layers (as a hybrid reverberant layer) is obtained from homomorphic analysis as a sum of the two echo delay times, that is $\tilde{\tau}_i$+$\tilde{\tau}_s$ = 4.5 s. We can see from the RF traces that the conversion phases associated with the sediment-crust interface have the largest amplitudes, while the Ps conversion at the Moho shows much lower amplitudes and its multiples are hardly visible (Figure 11b).

In this scenario, the autocorrelation analysis shows strong reverberation behavior with an echo number of k_d = 34.43 (Figure 11c), however, the estimated echo delay time of 1.47 s does not match any of the individual layer values ($\tilde{\tau}_i$, $\tilde{\tau}_s$, or $\tilde{\tau}_i$+$\tilde{\tau}_s$). The complex cepstrum, however, shows clear repeating negative and positive peaks (Figure 11d), indicating the presence of strong echoes in the data. A stack for the relevant echo-delay time gives a strong detection at 4.5 s (Figure 11e). This value matches that of the sum for both the ice and sediment layers. In the synthetic RF traces, the strong sediment phases at ~ 4.0 s are clearly repeated multiple times, separated by this interval (arrows in Figure 11b), visually confirming detection parameters of the homomorphic analysis.

To make these discoveries concrete, we apply the homomorphic analysis to teleseismic data collected from 18 stations deployed on the Antarctica glacier (Figure 12a). We obtain the echo delay times at each station from the stack of complex cepstrums of the receiver functions, and compare them with predicted ice-only echo delay times calculated using ice thicknesses obtained from the analysis of seismic data presented by (Phạm & Tkalčić, 2018). Their results are obtained from autocorrelation of radial and vertical seismograms, to extract the single-layer ice response. Our obtained echo delay times generally agree with those calculated from results from (Phạm & Tkalčić, 2018), with an average difference of 11.7%. In some cases, we

detect longer echo delay times (11 of 18 stations), which possibly indicates reverberations generated not only from the ice sheets, but also from the sedimentary layer beneath (Figure 12b).

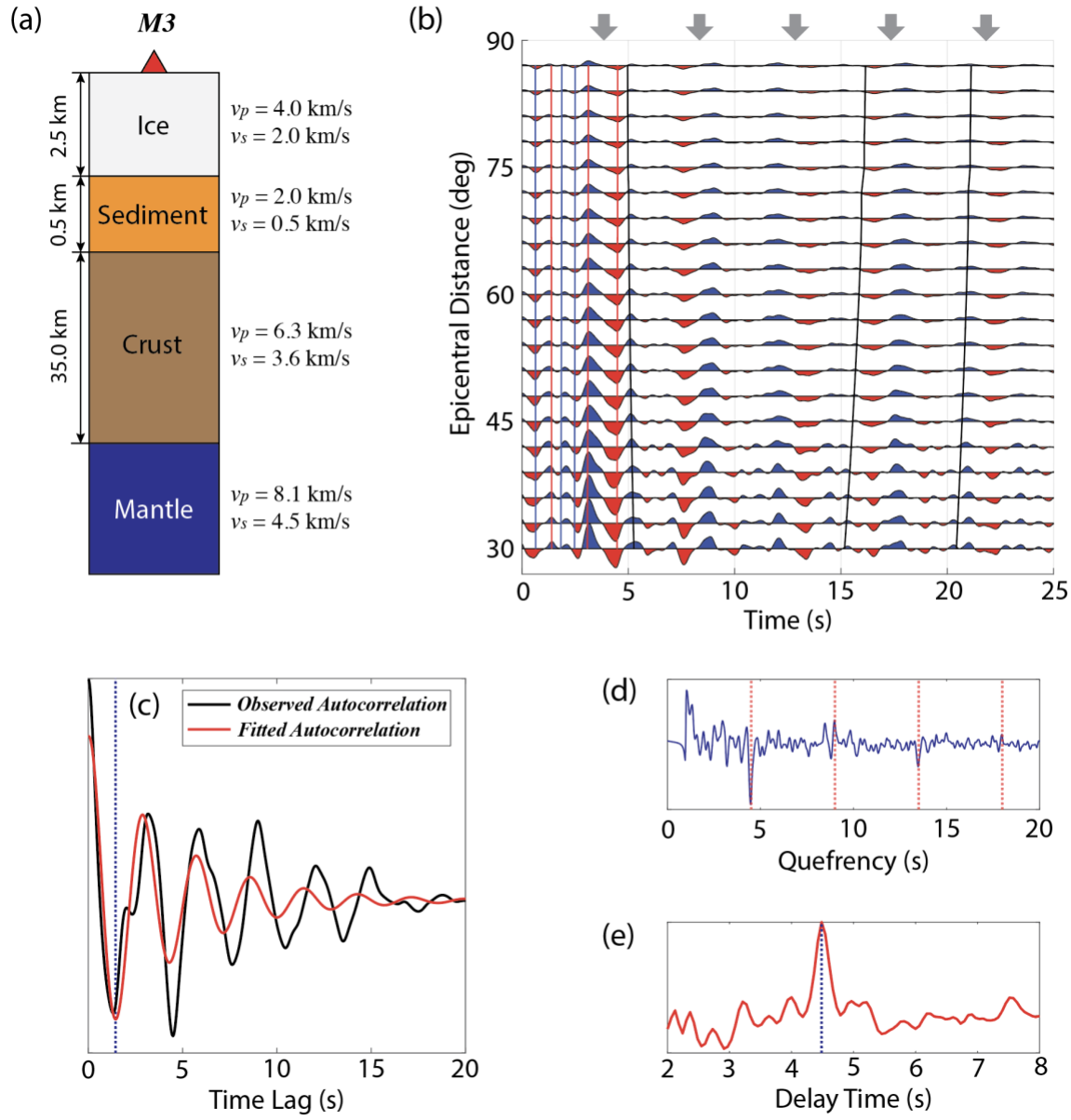

Figure 11. Synthetic experiment on echo detection when both ice and sediment layer present. (a) Layered model (M3) consisting of an ice layer, a sediment layer, a crustal layer, and a mantle half-space. (b) Synthetic RFs and theoretical arrivals of Ps conversions and their multiples associated with the bottom of ice, sediment, and crust (Blue, red, and black vertical lines, respectively). (c) Observed and fitted autocorrelation curves showing the estimated echo delay time (black dashed line), which does not match the input model. (d) Complex cepstrum and repeating quefrency peaks (red dashed lines) (e) Linear stack for the correct echo delay time (blue dashed line). The observed autocorrelation and the complex cepstrum are computed from the synthetic receiver functions in b. The signature of the repeating echoes detected by homomorphic analysis can be seen as doublets (marked by gray arrow in b).

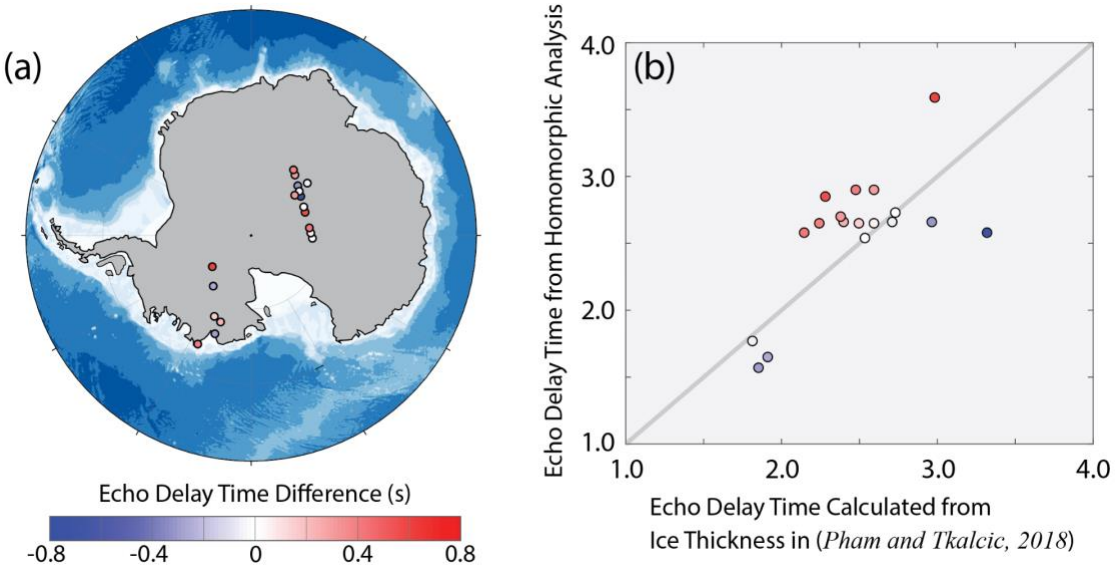

564

565 **Figure 12**. Comparison of echo delay times in Antarctica using homomorphic analysis (this study) with those calculated for
566 ice thicknesses derived from elastic structure estimated by (Phạm & Tkalčić, 2018). (a) Locations of the stations (circles) and
567 the estimated echo delay time difference (filled colors). (b) A comparison of our measured echo delay times (vertical axis) and
568 those for ice (horizontal axis), calculated from (Phạm & Tkalčić, 2018). We refer the readers to Table S3 in supporting
569 information for the detailed results of the absolute echo delay times.

570

571 ## 5.0 Discussions

572 ### 5.1 Fast and Automated Detection and Elimination of Echoes and Reverberations

573 In this study, we utilized both autocorrelation and homomorphic analysis to detect and
574 eliminate the effect of reverberations from teleseismic body wave signals. We note that
575 although this type of reverberation is but one of many classes of resonant seismic noise
576 (Hellweg, 2000; Roman, 2017), it differs from stationary harmonic noise in that it is signal-
577 generated, time-limited, and methods for removing stationary harmonic noise are not
578 appropriately suited for its elimination (Zali et al., 2021). In order to emphasize the receiver-
579 side reverberation response, we use an input receiver function signal obtained by
580 preprocessing the seismogram through source-deconvolution. In the case when only a single
581 channel sensor is available i.e, acoustic sensors like MERMAID (Pipatprathanporn & Simons,
582 2021; Simon et al., 2021), other source normalization techniques might be necessary to achieve
583 a similar effect (Bensen et al., 2007; Shen et al., 2012; Tkalčić et al., 2020).

584

585 In the single-layer scenario where reverberations are generated solely from a sedimentary layer,
586 or in the decoupled water-sediment system (Figures 7 & 10), an automated workflow can be

assembled based on the approach we outlined (Figures 2). The input source-deconvolved signal (i.e., receiver function) is first passed into the autocorrelation analysis to determine the presence and strength of reverberations. With a threshold for the echo number appropriately defined, this process can be performed automatically. An estimate of the parameters of the reverberation response, r_0 and $\tilde{\tau}_1$, is also obtained in this step. If reverberations are detected, the input signal is further analyzed by the homomorphic analysis, where an appropriate search window for the cepstral stack is determined by using $\tilde{\tau}_1 \pm \Delta\tau$. If the output echo delay time from this second step ($\tilde{\tau}_2$) agrees with the previous one ($\tilde{\tau}_1$), an average of the two can be taken as the final echo delay time. If they are off by a prescribed tolerance, the analyst can visually inspect the underlying autocorrelation curves or the complex cepstrum stacks (Figures 3 and 5) to judge which of these is more reliable, and decide if further data processing is necessary. The resonance removal filter can then be designed to remove the reverberation response from the input signal, using the estimated filter parameters. In the non-acoustic case where the seismic sensor is on the bottom of the ocean, the water reverberations are negligible due to their longer delay time and the lower transmission onto the radial seismogram (Zhang & Olugboji, 2021).

In an alternative application only detection and not elimination might be required (i.e., sections 3.2 and 3.3). An example is investigating if the reverberations do not affect late arriving conversions where $k_d << t_{Ps}$ from a specific lithospheric discontinuity (underplated crust or mantle layering). The aforementioned workflow can be easily adapted to perform this task, with the input being receiver functions from each station and the output being the echo number (k_d) and the consequent echo quality factor (Q_e), which determines the presence and strength of the reverberations. In this application, the workflow is still automated, and only autocorrelation analysis is used. Since our proposed workflow uses autocorrelation analysis to detect echoes, it may fail when a complicated seismic structure exists, i.e., in ice-sediment systems (see section 4). In this case, we recommend using the homomorphic analysis. When supplemented with a crude estimation of local ice and sediment thickness and shear velocity, if any, it can provide information on how to interpret the signature of the hybrid reverberation response.

617 **5.2 Homomorphic Deconvolution of the Reverberation Response**

618 As we have demonstrated extensively, homomorphic analysis is an effective approach to
619 identifying the signature of echoes in the sampled signals. Since the homomorphic
620 transformation maps convolution into addition, one might expect that a natural extension to
621 removing the reverberation response would be to subtract the cepstral peaks associated with
622 reverberations in the quefrency domain and calculate the inverse complex cepstrum, which
623 recovers the original signal. This is the case known as homomorphic deconvolution. This
624 approach to removing unwanted convolutional components from the time series has already
625 been explored for removing synthetic reverberations and seismic source deconvolution (Stoffa
626 et al., 1974; Ulrych, 1971). However, it has been pointed out that several factors, i.e., low-
627 frequency assumption of the source, compromised estimation in phase unwrapping, and the
628 presence of additive noise, make it unstable for practical applications (Bostock & Sacchi, 1997;
629 Clayton & Wiggins, 1976). Although homomorphic deconvolution is not used for
630 reverberation elimination in this study, we present a synthetic experiment here to demonstrate
631 its principles and shortcomings.
632
633 We generate a signal using a series of spike functions that put peaks and troughs at 1 s, 5 s,
634 and 6 s (Figure 13a). We then convolve this signal with a reverberation series consisting of ten
635 echoes (n = 10), with a reflection coefficient of r_0 = 0.6 and an echo delay time of $\tilde{\tau}$ = 1.0 s
636 (Figure 13b). The complex cepstrum is then calculated by the homomorphic analysis described
637 in section 2.2 (Figure 13c). Cepstral peaks are clearly visible at a 1.0 s quefrency interval, with
638 the first three especially profound. These three peaks are removed from the complex cepstrum
639 trace by setting the amplitudes to the average of their neighboring points (Figure 13d).
640

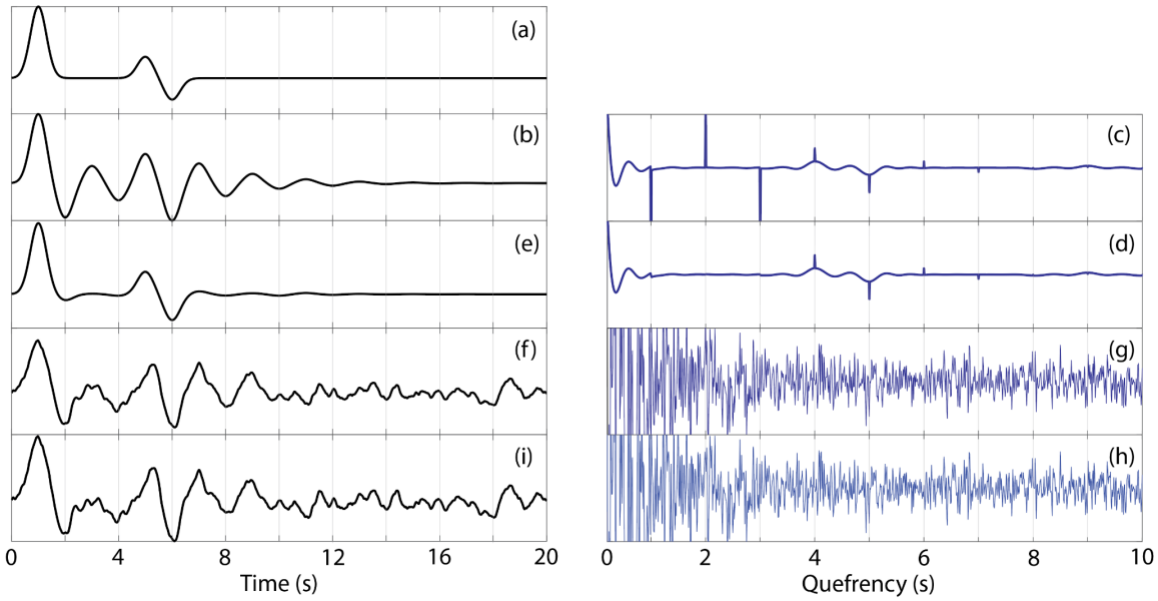

Figure 13. Homomorphic deconvolution with synthetic sampled signals. (a) Reference sampled signal generated by spike functions. (b) Signal in Figure 11a with reverberation. (c) Complex cepstrum of reverberated signal in Figure 11b. (d) Complex cepstrum shown in Figure 11c with the first three cepstral peaks removed. (e) Recovered time-domain signal from the inverse cepstrum transform of the complex transform in Figure 11d. (f) Signal in Figure 11b with additive noise added. (g) Complex cepstrum of reverberated signal in Figure 11f. (h) Complex cepstrum shown in Figure 11g with the first three theoretical cepstral peaks removed. (i) Recovered time-domain signal from the inverse cepstrum transform of the complex transform in Figure 11h.

We then perform an inverse cepstrum transform, which is the complex exponential of the Fourier transform of the complex cepstrum ($\hat{x} \xrightarrow{\mathcal{H}^{-1}} x$). The resulting signal is nearly identical to the reference signal, even though we only remove the first three, but not all the cepstral peaks in the quefrency domain (Figure 13e). However, with strong additive noise added to the sampled signal (Figure 13f), the complex cepstrum shows a much more complicated pattern and the theoretical cepstral peaks, which are supposed to show up at a 1.0 s interval, are hardly visible (Figure 13g). Since the noise is additive, not convolutional, the homomorphic transform cannot separate it from the clean signal spectrum, and thus, result in a very noisy complex cepstrum. With no surprise, averaging the theoretical cepstral peaks results in an almost identical noisy cepstrum trace (Figure 13h) and can no longer recover the original signal with inverse cepstrum transform (Figure 13i).

6.0 Conclusion

In this study, we have addressed the problem of high-resolution imaging of the crust and mantle lithosphere using the teleseismic body-wavefield that suffers severe distortion from complex scattering through reverberant structures - sediments, oceans and glaciers. We develop an automated technique for identifying the signature and strength of reverberations and to eliminate its negative effect. We do this by extending and applying autocorrelation and homomorphic analysis to detection, and robust filter design, enabling the deconvolution of the reverberation response. We demonstrate, using synthetic experiments, that our approach is effective in a wide variety of scenarios. Real data examples, with seismic arrays in the Upper Mississippi Embayment and the Aleutian subduction zone, shows that detection and elimination of reverberations should be conducted routinely before the interpretation of results for subsurface lithospheric layering. In the more complicated environment of glaciers, where both ice and sediment are present, homomorphic analysis is preferred. We anticipate application of our workflow across a variety of seismic deployments where the reverberation challenge has limited the utility of teleseismic body wave data for lithospheric imaging.

7.0 Data Availability Statement

All seismic data used in this study can be obtained from the IRIS Data management center (https://ds.iris.edu/ds) under the network codes YP (station NE68), TA (Earthscope transportable array stations in the UME), XO (the Alaska amphibious community seismic experiment, AACSE), YT and ZM (Antarctica). Synthetic receiver functions were computed using the Telewavesim open-source python library provided by (Audet et al., 2019). The receiver function deconvolution was computed using compiled C++ code provided by (Olugboji & Park, 2016). The MatLab code for fitting a decaying sinusoid can be retrieved from (Amberg, 2022). The MatLab package of the proposed workflow for Fast and Automated Detection and Elimination of Echoes and Reverberations (FADER) can be retrieved from (Zhang & Olugboji, 2022).

8.0 Acknowledgements

This work was made possible by grants and support from the National Science Foundation under grant number: 1818654. The authors acknowledge the use of the BlueHive Linux cluster

694 at the University of Rochester's Center for Integrated Research Computing, CIRC
695 (https://www.circ.rochester.edu/). The authors acknowledge many helpful discussions with
696 Jean-Joel Legre, Steve Carr, Siyu Xue, Walter Hennings, Xinxuan Lu, Enting Zhou, Baowei
697 Liu, Zhiyao Duan, Ge Zhu, and Yujia Yan.

References Cited

Akuhara, T., & Mochizuki, K. (2015). Hydrous state of the subducting Philippine Sea plate inferred from receiver function image using onshore and offshore data. *Journal of Geophysical Research, [Solid Earth]*, *120*(12), 8461–8477. https://doi.org/10.1002/2015JB012336

Akuhara, T., Mochizuki, K., Kawakatsu, H., & Takeuchi, N. (2016). Non-linear waveform analysis for water-layer response and its application to high-frequency receiver function analysis using OBS array. *Geophysical Journal International*, *206*(3), 1914–1920. https://doi.org/10.1093/gji/ggw253

Amberg, D. (2022). *Fit a damped sine wave* [MATLAB Central File Exchange]. Retrieved from https://www.mathworks.com/matlabcentral/fileexchange/50756-fit-a-damped-sine-wave

Anandakrishnan, S., Voigt, D. E., Burkett, P. G., Long, B., & Henry, R. (2000). Deployment of a broadband seismic network in west Antarctica. *Geophysical Research Letters*, *27*(14), 2053–2056. https://doi.org/10.1029/1999gl011189

Audet, P. (2016). Receiver functions using OBS data: promises and limitations from numerical modelling and examples from the Cascadia Initiative. *Geophysical Journal International*, *205*(3), 1740–1755. https://doi.org/10.1093/gji/ggw111

Audet, P., Thomson, C., Bostock, M., & Eulenfeld, T. (2019). Telewavesim: Python software for teleseismic body wave modeling. *Journal of Open Source Software*, *4*(44), 1818. https://doi.org/10.21105/joss.01818

Backus, M. M. (1959). WATER REVERBERATIONS—THEIR NATURE AND ELIMINATION. *Geophysics*, *24*(2), 233–261. https://doi.org/10.1190/1.1438579

Barcheck, G., Abers, G. A., Adams, A. N., Bécel, A., Collins, J., Gaherty, J. B., et al. (2020). The Alaska Amphibious Community Seismic Experiment. *Bulletin of the Seismological Society of America*, *91*(6), 3054–3063. Retrieved from https://pubs.geoscienceworld.org/ssa/srl/article-pdf/91/6/3054/5176819/srl-2020189.1.pdf

Bees, Blostein, & Kabal. (1991). Reverberant speech enhancement using cepstral processing. In *Acoustics, Speech, and Signal Processing, IEEE International Conference on* (Vol. 0, pp. 977–980). computer.org. https://doi.org/10.1109/ICASSP.1991.150504

Bensen, G. D., Ritzwoller, M. H., Barmin, M. P., Levshin, a. L., Lin, F., Moschetti, M. P., et al. (2007). Processing seismic ambient noise data to obtain reliable broad-band surface wave dispersion measurements. *Geophysical Journal International*, *169*(3), 1239–1260. https://doi.org/10.1111/j.1365-246X.2007.03374.x

Blankenship, D. D., Bell, R. E., Hodge, S. M., Brozena, J. M., Behrendt, J. C., & Finn, C. A. (1993). Active volcanism beneath the West Antarctic ice sheet and implications for ice-sheet stability. *Nature*, *361*(6412), 526–529. https://doi.org/10.1038/361526a0

Bogert, B. P., Healy, M. J. R., & Tukey, J. W. (1963). The quefrency alanysis of time series for echoes ; Cepstrum, pseudo-autocovariance, cross-cepstrum and saphe cracking. *Time Series Analysis*, 209–243. Retrieved from https://ci.nii.ac.jp/naid/10006519906/

Bonner, J. L., Reiter, D. T., & Shumway, R. H. (2002). Application of a Cepstral F Statistic for Improved Depth Estimation. *Bulletin of the Seismological Society of America*, *92*(5), 1675–1693. https://doi.org/10.1785/0120010128

Bostock, M. G., & Sacchi, M. D. (1997). Deconvolution of teleseismic recordings for mantle structure. *Geophysical Journal International*, *129*(1), 143–152. https://doi.org/10.1111/j.1365-246X.1997.tb00943.x

Bostock, M. G., & Tréhu, A. M. (2012). Wave-Field Decomposition of Ocean Bottom Seismograms. *Bulletin of the Seismological Society of America*, *102*(4), 1681–1692. https://doi.org/10.1785/0120110162

Buhl, P., Stoffa, P. L., & Bryan, G. M. (1974). The application of homomorphic deconvolution to Shallow-Water marine seismology—part ii: Real data. *Geophysics*, *39*(4), 417–426. https://doi.org/10.1190/1.1440439

Chai, C., Ammon, C. J., Anandakrishnan, S., Ramirez, C., & Nyblade, A. (2017). Estimating subglacial structure using P-

wave receiver functions. *Geophysical Journal International*, *209*(2), 1064–1079. https://doi.org/10.1093/gji/ggx075

Chaput, J., Aster, R. C., Huerta, A., Sun, X., Lloyd, A., Wiens, D., et al. (2014). The crustal thickness of West Antarctica. *Journal of Geophysical Research, [Solid Earth]*, *119*(1), 378–395. https://doi.org/10.1002/2013jb010642

Childers, D. G., Skinner, D. P., & Kemerait, R. C. (1977). The cepstrum: A guide to processing. *Proceedings of the IEEE*, *65*(10), 1428–1443. https://doi.org/10.1109/PROC.1977.10747

Cho, T. (2011). Removing Reverberation in Ice Sheets from Receiver Functions. *Seismological Research Letters*, *82*(2), 207–210. https://doi.org/10.1785/gssrl.82.2.207

Clayton, R. W., & Wiggins, R. A. (1976). Source shape estimation and deconvolution of teleseismic bodywaves. *Geophysical Journal International*, *47*(1), 151–177. https://doi.org/10.1111/j.1365-246X.1976.tb01267.x

Clinton, J. F., Nettles, M., Walter, F., Anderson, K., Dahl-Jensen, T., Giardini, D., et al. (2014). Seismic network in Greenland monitors earth and ice system. *Eos*, *95*(2), 13–14. https://doi.org/10.1002/2014eo020001

Cohen, T. J. (1970). Source-Depth Determinations using Spectral, Pseudo-Autocorrelation and Cepstral Analysis. *Geophysical Journal International*, *20*(2), 223–231. https://doi.org/10.1111/j.1365-246X.1970.tb06065.x

Cunningham, E., & Lekic, V. (2019). Constraining crustal structure in the presence of sediment: a multiple converted wave approach. *Geophysical Journal International*, *219*(1), 313–327. https://doi.org/10.1093/gji/ggz298

Deng, L., Droppo, J., & Acero, A. (2004). Estimating cepstrum of speech under the presence of noise using a joint prior of static and dynamic features. *IEEE Transactions on Audio, Speech, and Language Processing*, *12*(3), 218–233. https://doi.org/10.1109/TSA.2003.822627

Eberhart-Phillips, D., & Christensen, D. H. (2006). Imaging the transition from Aleutian subduction to Yakutat collision in central Alaska, with local earthquakes and active source data. *Journal of*. https://doi.org/10.1029/2005JB004240

Fahnestock, M., Abdalati, W., Joughin, I., Brozena, J., & Gogineni, P. (2001). High Geothermal Heat Flow, Basal Melt, and the Origin of Rapid Ice Flow in Central Greenland. *Science*, *294*(5550), 2338–2342. https://doi.org/10.1126/science.1065370

Graw, J. H., Hansen, S. E., Langston, C. A., Young, B. A., Mostafanejad, A., & Park, Y. (2017). An Assessment of Crustal and Upper-Mantle Velocity Structure by Removing the Effect of an Ice Layer on the P-Wave Response: An Application to Antarctic Seismic Studies. *Bulletin of the Seismological Society of America*, *107*(2), 639–651. Retrieved from https://pubs.geoscienceworld.org/ssa/bssa/article-abstract/107/2/639/354175

Hellweg, M. (2000). Physical models for the source of Lascar's harmonic tremor. *Journal of Volcanology and Geothermal Research*, *101*(1), 183–198. https://doi.org/10.1016/S0377-0273(00)00163-3

Janiszewski, H. A., & Abers, G. A. (2015). Imaging the Plate Interface in the Cascadia Seismogenic Zone: New Constraints from Offshore Receiver Functions. *Seismological Research Letters*, *86*(5), 1261–1269. https://doi.org/10.1785/0220150104

Kawakatsu, H., & Utada, H. (2017). Seismic and Electrical Signatures of the Lithosphere–Asthenosphere System of the Normal Oceanic Mantle. *Annual Review of Earth and Planetary Sciences*, *45*(1), 139–167. https://doi.org/10.1146/annurev-earth-063016-020319

Kumar, P., Kind, R., Priestley, K., & Dahl-Jensen, T. (2007). Crustal structure of Iceland and Greenland from receiver function studies. *Journal of Geophysical Research*, *112*(B3). https://doi.org/10.1029/2005jb003991

Langston, C. A. (2011). Wave-field continuation and decomposition for passive seismic imaging under deep unconsolidated sediments. *Bulletin of the Seismological Society of America*, *101*(5), 2176–2190. https://doi.org/10.1785/0120100299

Laske, G., Collins, J. A., & Wolfe, C. J. (2009). Probing the Hawaiian hot spot with new broadband ocean bottom instruments. *Eos, Transactions, American Geophysical Union* . Retrieved from https://agupubs.onlinelibrary.wiley.com/doi/abs/10.1029/2009EO410002

781 Letort, J., Bollinger, L., Lyon-Caen, H., Guilhem, A., Cano, Y., Baillard, C., & Adhikari, L. B. (2016). Teleseismic depth
782 estimation of the 2015 Gorkha−Nepal aftershocks. *Geophysical Journal International*, *207*(3), 1584–1595.
783 https://doi.org/10.1093/gji/ggw364
784 Letort, J., Trilla, A. G., Ford, S. R., & Myers, S. C. (2018). Multiobjective Optimization of Regional and Teleseismic Data to
785 Constrain the Source of the 12 September 2016 M w 5.4 Earthquake in South Korea. *Bulletin of the Seismological Society of*
786 *America*, *108*(1), 175–187. Retrieved from https://pubs.geoscienceworld.org/ssa/bssa/article-
787 abstract/108/1/175/524870
788 Liu, L., Gao, S. S., Liu, K. H., & Mickus, K. (2017). Receiver function and gravity constraints on crustal structure and
789 vertical movements of the Upper Mississippi Embayment and Ozark Uplift. *Journal of Geophysical Research, [Solid Earth]*,
790 *122*(6), 4572–4583. https://doi.org/10.1002/2017jb014201
791 Olugboji, T. M., & Park, J. (2016). Crustal anisotropy beneath Pacific Ocean-Islands from harmonic decomposition of
792 receiver functions. *Geochemistry, Geophysics, Geosystems*, *17*(3), 810–832. https://doi.org/10.1002/2015GC006166
793 Olugboji, T. M., Karato, S.-I., & Park, J. (2013). Structures of the oceanic lithosphere-asthenosphere boundary: Mineral-
794 physics modeling and seismological signatures. *Geochemistry, Geophysics, Geosystems*, *14*(4), 880–901. Retrieved from
795 https://agupubs.onlinelibrary.wiley.com/doi/abs/10.1002/ggge.20086
796 Oppenheim, A. V. (1969). Speech analysis-synthesis system based on homomorphic filtering. *The Journal of the Acoustical*
797 *Society of America*, *45*(2), 458–465. https://doi.org/10.1121/1.1911395
798 Oppenheim, A. V., & Schafer, R. W. (2004). From frequency to quefrency: A history of the cepstrum. *IEEE Signal Processing*
799 *Magazine*, *21*(5), 95–106. Retrieved from https://ieeexplore.ieee.org/abstract/document/1328092/
800 Park, J., & Levin, V. (2000). Receiver functions from multiple-taper spectral correlation Estimates. *Bulletin of the Seismological*
801 *Society of America*, *90*(6), 1507–1520. https://doi.org/10.1785/0119990122
802 Park, J., & Levin, V. (2016). Statistics and frequency-domain moveout for multiple-taper receiver functions. *Geophysical*
803 *Journal International*, *207*(1), 512–527. https://doi.org/10.1093/gji/ggw291
804 Phạm, T.-S., & Tkalčić, H. (2018). Antarctic ice properties revealed from teleseismic P wave coda autocorrelation. *Journal of*
805 *Geophysical Research, [Solid Earth]*, *123*(9), 7896–7912. https://doi.org/10.1029/2018jb016115
806 Pipatprathanporn, S., & Simons, F. J. (2021). One year of sound recorded by a mermaid float in the Pacific: hydroacoustic
807 earthquake signals and infrasonic ambient noise. *Geophysical Journal International*, *228*(1), 193–212.
808 https://doi.org/10.1093/gji/ggab296
809 Roman, D. C. (2017). Automated detection and characterization of harmonic tremor in continuous seismic data. *Geophysical*
810 *Research Letters*, *44*(12), 6065–6073. https://doi.org/10.1002/2017gl073715
811 Rychert, C., Harmon, N., Constable, S., & Wang, S. (2020). The nature of the Lithosphere-Asthenosphere Boundary. *Journal*
812 *of Geophysical Research, [Solid Earth]*. https://doi.org/10.1029/2018JB016463
813 Scheuer, T. E., & Wagner, D. E. (1985). Deconvolution by autocepstral windowing. *Geophysics*, *50*(10), 1533–1540.
814 https://doi.org/10.1190/1.1441843
815 Shen, W., Wiens, D. A., Anandakrishnan, S., Aster, R. C., Gerstoft, P., Bromirski, P. D., et al. (2018). The crust and upper
816 mantle structure of central and west Antarctica from Bayesian inversion of Rayleigh wave and receiver functions.
817 *Journal of Geophysical Research, [Solid Earth]*, *123*(9), 7824–7849. https://doi.org/10.1029/2017jb015346
818 Shen, Y., Ren, Y., Gao, H., & Savage, B. (2012). An improved method to extract very-broadband empirical green's
819 functions from ambient seismic noise. *Bulletin of the Seismological Society of America*, *102*(4), 1872–1877.
820 https://doi.org/10.1785/0120120023
821 Shillington, D. J., Van Avendonk, H. J. A., Holbrook, W. S., Kelemen, P. B., & Hornbach, M. J. (2004). Composition and
822 structure of the central Aleutian island arc from arc-parallel wide-angle seismic data. *Geochemistry, Geophysics, Geosystems*,

5(10). https://doi.org/10.1029/2004gc000715

Simon, J. D., Simons, F. J., & Irving, J. C. E. (2021). Recording earthquakes for tomographic imaging of the mantle beneath the South Pacific by autonomous MERMAID floats. *Geophysical Journal International*, *228*(1), 147–170. https://doi.org/10.1093/gji/ggab271

Stoffa, P. L., Buhl, P., & Bryan, G. M. (1974). THE APPLICATION OF HOMOMORPHIC DECONVOLUTION TO SHALLOW-WATER MARINE SEISMOLOGY—PART I: MODELS. *Geophysics*, *39*(4), 401–416. https://doi.org/10.1190/1.1440438

Suetsugu, D., & Shiobara, H. (2014). Broadband Ocean-Bottom Seismology. *Annual Review of Earth and Planetary Sciences*, *42*(1), 27–43. https://doi.org/10.1146/annurev-earth-060313-054818

Suetsugu, D., Shiobara, H., Sugioka, H., Tada, N., Ito, A., Isse, T., et al. (2018). The OJP array: seismological and electromagnetic observation on seafloor and islands in the Ontong Java Plateau. *JAMSTEC Report of Research and Development*, *26*, 54–64. https://doi.org/10.5918/jamstecr.26.54

Tao, K., Liu, T., Ning, J., & Niu, F. (2014). Estimating sedimentary and crustal structure using wavefield continuation: theory, techniques and applications. *Geophysical Journal International*, *197*(1), 443–457. https://doi.org/10.1093/gji/ggt515

Tkalčić, H., Phạm, T.-S., & Wang, S. (2020). The Earth's coda correlation wavefield: Rise of the new paradigm and recent advances. *Earth-Science Reviews*, *208*, 103285. https://doi.org/10.1016/j.earscirev.2020.103285

Ulrych, T. J. (1971). Application of homomorphic deconvolution to seismology. *Geophysics*, *36*(4), 650–660. https://doi.org/10.1190/1.1440202

Wear, K. A., Wagner, R. F., Insana, M. F., & Hall, T. J. (1993). Application of autoregressive spectral analysis to cepstral estimation of mean scatterer spacing. *IEEE Transactions on Ultrasonics, Ferroelectrics, and Frequency Control*, *40*(1), 50–58. https://doi.org/10.1109/58.184998

Wiens, D. A., Shen, W., & Lloyd, A. J. (2021). The seismic structure of the Antarctic upper mantle. *Geological Society, London, Memoirs*, *56*. https://doi.org/10.1144/M56-2020-18

Yu, Y., Song, J., Liu, K. H., & Gao, S. S. (2015). Determining crustal structure beneath seismic stations overlying a low-velocity sedimentary layer using receiver functions: RECEIVER FUNCTION CRUSTAL STUDY. *Journal of Geophysical Research, [Solid Earth]*, *120*(5), 3208–3218. https://doi.org/10.1002/2014JB011610

Zali, Z., Ohrnberger, M., Scherbaum, F., Cotton, F., & Eibl, E. P. S. (2021). Volcanic Tremor Extraction and Earthquake Detection Using Music Information Retrieval Algorithms. *Seismological Research Letters*, *92*(6). https://doi.org/10.1785/0220210016

Zelt, B. C., & Ellis, R. M. (1999). Receiver-function studies in the Trans-Hudson Orogen, Saskatchewan. *Canadian Journal of Earth Sciences*, *36*(4), 585–603. https://doi.org/10.1139/e98-109

Zhang, Z., & Olugboji, T. (2021). The signature and elimination of sediment reverberations on submarine receiver functions. *Journal of Geophysical Research, [Solid Earth]*, *126*(5). https://doi.org/10.1029/2020jb021567

Zhang, Z., & Olugboji, T. (2022). *URseismology/FADER: v0.1.0*. https://doi.org/10.5281/zenodo.6804873